

A Deep Learning Framework for Single-Sided Sound Speed Inversion in Medical Ultrasound

Micha Feigin, Daniel Freedman, and Brian W. Anthony

Abstract—Objective: Ultrasound elastography is gaining traction as an accessible and useful diagnostic tool for such things as cancer detection and differentiation and thyroid disease diagnostics. Unfortunately, state of the art shear wave imaging techniques, essential to promote this goal, are limited to high end ultrasound hardware due to high power requirements; are extremely sensitive to patient and sonographer motion; and generally suffer from low frame rates.

Motivated by research and theory showing that pressure wave velocity carries similar diagnostic abilities to shear wave imaging, we present an alternative approach using single sided pressure-wave velocity measurements from a conventional ultrasound probe, enabling elasticity based diagnostics using portable and low cost devices.

Methods: In this paper, we present a single sided sound speed inversion solution using a fully convolutional deep neural network. We use simulations for training, allowing the generation of large volumes of ground truth data.

Results: We show that it is possible to invert for longitudinal sound speed in soft tissue at super real time frame rates. Our method shows exceptional results on simulated data, and highly encouraging initial results on real data.

Conclusion: Sound speed inversion on channel data has significant potential, made possible in real time with deep learning technologies.

Significance: High end ultrasound devices remain inaccessible in many locations. Utilizing pressure sound speed and deep learning technologies, brings the same quality diagnostic abilities to low power devices at real time frame rates. Potential frame rates also enable dynamic functional imaging, impossible with shear wave imaging.

Index Terms—Deep learning, Inverse problems, Ultrasound, Sound Speed inversion

I. INTRODUCTION

Abnormalities in mechanical tissue properties, tissue structures, and the spatial arrangement of properties and structures are useful in disease diagnosis in various organs, including the kidneys [1], [2], thyroid, muscle, breast [3], [4], liver [5], [6], and prostate. Tracking changes to tissue properties, tissue structure, and the spatial distribution of both is useful for monitoring disease progression as well as response to therapeutic interventions.

Embedded in ultrasound signals is information about the mechanical (and acoustic) properties of the tissue through which the ultrasound waves have propagated or from which ultrasound waves have been reflected. Properties include the

This work has been submitted to the IEEE for possible publication. Copyright may be transferred without notice, after which this version may no longer be accessible.

M. Feigin and B. W. Anthony are with the Department of Mechanical Engineering, Massachusetts Institute of Technology, Cambridge, MA, USA.

D. Freedman is with Google Research, Haifa, Israel.

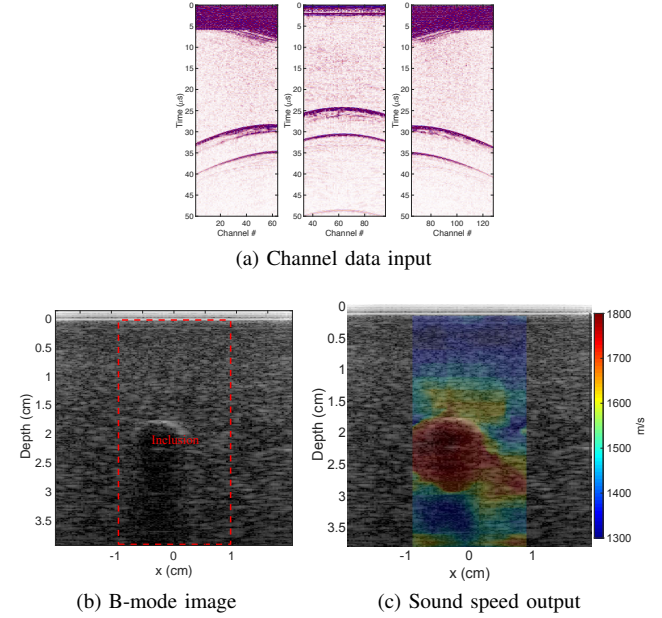


Fig. 1. Goal: the target of this work is to be able to take raw ultrasound channel data (a) and in addition to the standard B-mode image (b), also produce the corresponding tissue sound speed map (c)

longitudinal-wave speed of sound, shear-wave speed of sound, tissue density, attenuation, shear modulus, and bulk modulus. As part of the classical B-mode imaging process however, significant parts of this information are discarded through the application of beam forming (delay and sum focusing) and envelope detection.

The ability to provide diagnostically relevant physical measurements in real time is highly enticing, and can greatly assist the physician's workflow. All the more so, if these measurements can be produced on low cost hardware, and not be limited to high end ultrasound devices. It will improve real time decision making for experts while at the same time make high level of care more accessible in locations where direct access to experts is limited, such as the developing world and rural areas.

The past several years have seen a burst of interest in the use of AI for improving the physician's work flow, from automatic analysis and improvement of medical images to incorporating medical data and physician notes into diagnostics. Considerable research has gone into analyzing image attributes for the purpose of using them as disease biomarkers. However, the vast majority of this research effort has taken the imaging process itself as given, and has focused on processing

the images coming from the fixed process. There has been considerably less work on the use of Deep Learning for the inverse problem applied to raw signals, i.e. channel data.

In this work we exploit the information embedded in the raw ultrasound channel data signal. As depicted in Fig. 1, we take ultrasound channel data and generate the sound speed map of the tissue, without going through an imaging or beam-forming step. This resulting information is invaluable both directly for diagnostic purposes, as well as indirectly, for improving the image formation process and final image quality. To achieve this end, we harness the power of deep convolutional neural networks. We present exceptional results on simulation data as well as encouraging initial results on real data.

This work is the first step towards implementing a full waveform solver for recovering more general elastic and viscoelastic tissue parameters using Deep Learning, and shows the viability of this framework to such applications. Despite numerous applications of various inverse problem between different image domains, this is the first implementation we are aware of which applies a Deep Learning framework to raw time domain RF type signals. This is also the first solution we are aware of that works toward single-sided full waveform inversion in the ultrasound domain. We emphasize that the resulting technique works directly on a standard ultrasound probe.

A major advantage of our system is that it can work at real time frame rates, with the current implementation running at over 150fps on a single NVIDIA 1080Ti GPU. It requires only a small number of transmits, and can therefore run in parallel to standard imaging. More than that, the physical limitation on frame rates is on the order of 3000 frame per second. This opens the door to doing dynamic functional imaging.

II. BACKGROUND AND PRIOR WORK

As previously discussed, our end goal with this work is to measure a physical tissue property with direct diagnostic relevance. The current state of the art is shear wave elastography. The driving motivation is that shear wave velocity is directly related to the shear modulus, which in turn, under appropriate assumptions, to the Young's modulus.

We take an alternate route, as is taken by travel time tomography, to measure the pressure speed of sound. Under similar assumptions to shear wave elastography, pressure wave velocity is similarly related to the shear modulus, with the limitations that it is also controlled by the bulk modulus. Current research however shows that it contains similar diagnostic merit.

In this section, we start by giving a brief overview on the physics and techniques for shear wave elastography and tomographic ultrasound elastography. We continue by giving an overview of the clinical motivation for using these metrics for diagnostics. Finally, we give an overview of deep learning in the context of medical imaging.

A. Elastography and full waveform inversion

The currently prevailing model for ultrasound elastography of soft tissue is that of a linear isotropic elastic material. While

this does not account for non-linear effects, it is still useful for diagnostic purposes for most soft tissues, and can still be relatively easily extended to include the viscoelastic based attenuation by employing a complex sound speed.

Under this model, tissue properties can be described using density and two independent elastic coefficients. Some of the commonly used pairs are Young's modulus (E) and Poisson ratio (ν), bulk modulus (K) and shear modulus (G), and the two Lamme parameters (λ and μ). Note that the shear modulus and Lamme's second parameter are the same in this case. The Young's modulus is most often used to describe tissue stiffness, and is the value most closely related to what we intuitively perceive as material stiffness. The complementary elastic parameter, either the poison ratio or shear modulus, as well as the density, are often assumed to be constant, and dominated by the tissue's high water content.

The pressure wave (also known as p-wave, primary wave or longitudinal wave) is an acoustic wave used for ultrasound imaging, and travels at 1540 m/s on average in soft tissue. The shear wave (also known as s-wave, secondary wave or transverse wave) is measured indirectly in ultrasound elastography, using pressure waves, and is much slower. It travels at velocities on the order of 3 m/s in healthy tissue, and up to 60 m/s in highly pathological tissue. When working in the linear acoustics regime in soft tissue, as is the case for medical ultrasound imaging, the pressure waves and the two orthogonally polarized shear waves are independent, and only distinctly couple at strong discontinuities. This, together with the vast velocity difference between the two wave types, allows the use of pressure waves to image shear wave propagation, and is the basis for shear wave imaging.

Ultrasound shear wave imaging, is the currently deployed state of the art [7], [8], [9]. Common methods of shear wave generation include acoustic radiation force (ARFI) [8] and supersonic shear wave [10], [11]. A mechanical shear wave is generated in the tissue and its propagation velocity is tracked using pressure waves. Some devices return the actual measured shear wave velocity, while others approximate the Young's modulus by assuming that the Poisson ratio and mass density are fixed [12], [13] and using the relation

$$E = 2G(1 + \nu) \approx 3\rho C_{\text{shear}}^2. \quad (1)$$

With C_{shear} denoting the shear wave velocity. These methods however are limited to high end devices due to high power and probe requirements. They also generally suffer from low frame rates, long settling times, and high sensitivity to sonographer and subject motion.

Active research is being conducted on tomographic ultrasound imaging for travel time tomography and full waveform inversion, mostly focused on breast [14], [15], [16], [17], [18], [19], [20], and musculoskeletal [21], [22] imaging, both showing promising prospects. Current implementations in actual tissue, however, require a full circumferential field of view, limiting them to small body parts. Both are also extremely computationally expensive and sensitive to noise and choice of initial conditions.

Single-sided techniques are in use in the seismic domain, but usually require operator intervention for good results. Their

Brest tissue type	# of samples	Young's modulus (kPa) mean \pm STD
Normal fat	71	3.25 \pm 0.91
Normal fibroglandular tissue	26	3.24 \pm 0.61
Fibroadenoma	16	6.41 \pm 2.86
Low-grade IDC	12	10.40 \pm 2.60
ILC	4	15.62 \pm 2.64
DCIS	4	16.38 \pm 1.55
Fibrocystic disease	4	17.11 \pm 7.35
Intermediate-grade IDC	21	19.99 \pm 4.2
High-grade IDC	9	42.52 \pm 12.47
IMC	1	20.21
Fat necrosis	1	4.45

TABLE I

YOUNG'S MODULUS AS A DISEASE BIOMARKER FOR VARIOUS BREAST TISSUE TYPES [28], [29]

use in medical ultrasound imaging is limited, and is generally performed based on focusing techniques or PSF analysis on the final b-mode image, and not by an inversion method [23], [24], [25], [26], [27].

The motivation for both approaches can be derived from looking at the dependence of the shear wave velocity and pressure wave velocity on the underlying physical properties.

$$C_{\text{pressure}} = \sqrt{\frac{K + \frac{4}{3}G}{\rho}} \quad (2)$$

$$C_{\text{shear}} = \sqrt{\frac{G}{\rho}} \quad (3)$$

where C denotes the appropriate speed of sound. Under the previously stated assumption of a constant bulk modulus and density, at least to a first order approximation, both squared velocities depend linearly on the same single value, the shear modulus, in turn directly related to the value of interest, the Young's modulus.

B. Clinical motivation

Short of attaining fully automated diagnostics, the next best thing is to solve the inverse problem of measuring physical tissue properties. Focus is given to properties that can be used directly by the physician as reliable disease biomarkers. Achieving that end in an accessible and easily undertaken way can greatly improve the physician workflow as well as make quality health care much more accessible.

Current research is mostly split in two directions, shear wave elastography and ultrasound tomography, both travel time tomography and full waveform inversion. Table I presents Young's modulus values for several healthy and pathological breast tissues as given by [28], [29]. As can be seen, Young's modulus has strong predictive value for detecting and differentiating pathological tissue.

Researchers have also shown that pressure wave sound speed has similar diagnostic ability to shear wave imaging [30], [31], [32], [20], [33], [34]. Some of these results taken on breast tissue are presented in Table II (extracted from [32]).

Using longitudinal speed of sound as a substitute for transverse speed of sound presents several potential advantages. For starters, longitudinal waves travel significantly faster in tissue than transverse waves, allowing for much higher frame

Brest tissue type	Sound speed (m/s)
Normal fat	1442 \pm 9
Breast parenchyma	1487 \pm 21
Benign breast lesions	1513 \pm 27
Malignant breast lesions	1548 \pm 17

TABLE II

LONGITUDINAL SOUND SPEED AS A DISEASE BIOMARKER FOR VARIOUS BREAST TISSUE TYPES [32]

rates. Secondly, transverse waves cannot be detected directly on the probe, due to their strong attenuation in tissue along with low sensitivity of the Piezo sensors to transverse motion. As a result they are only imaged indirectly by their effect on longitudinal waves. The particle motion that is detected is on the order of 10 microns, resulting in measurements that are highly sensitive to probe and subject motion. The amount of energy required to generate shear waves using acoustic radiation force is also high, requiring correspondingly high powered devices. This in turn limits this technology to high end ultrasound machines; furthermore, frame rates must be lowered due to FDA limitations on transmission power and long settling times.

As a clinical imaging modality, ultrasound is different from modalities such as CT and MRI in that it uses non-ionizing radiation, is mobile, and has significantly lower purchase and operating costs than most other medical imaging alternatives. The mode of operation is also quite different, as an interactive exploratory approach is taken. The operator can move the probe around, vary applied pressure, and adapt to findings in real time, making real time quantitative diagnosis techniques that much more important. On the down side, different tissue types are not differentiated in the images, requiring more experience to interpret the images.

C. Deep Learning

The astounding success of Deep Learning in fields including computer vision, speech recognition, and natural language processing is by now widely known. Neural networks have achieved state of the art results on many benchmarks within each of these fields. In most cases, the networks in question are relatively deep (tens or hundreds of layers), and are trained by stochastic gradient descent or related techniques, as implemented by the standard backpropagation algorithm.

Deep Learning has also achieved great success in medical imaging on standard computer vision tasks, such as classification [35], detection [36], and segmentation [37]. However, it is only more recently that Deep Learning has been applied to problems in sensing and image reconstruction. The growing popularity of this trend is exemplified by the recent special issue (June 2018) of TMI which was devoted to this topic. The issue contained many papers related to both CT and MRI. Within the realm of CT, a variety of topics were examined, including artifact reduction [38], denoising [39], [40], and sparse-view [41], [42] and low-dose [43], [44] reconstruction. Papers on MRI tended to focus on Deep Learning approaches to compressive sensing [45], [46], [47]. Deep Learning has also been applied, though not quite as widely, to PET [48], [49] and Photoacoustic Tomography [50], [51]. Furthermore,

we note that in the broader signal processing community, work has been devoted to applying Deep Learning techniques to general reconstruction problems, such as compressive sensing [52] and phase retrieval [53].

Within the field of ultrasound, Deep Learning has been successfully employed in a few areas. Vedula *et al.* [54] train a multi-resolution CNN to generate CT quality images from raw ultrasound measurements. Yoon *et al.* [55] apply Deep Learning to produce B-mode images from a small number of measurements, which can circumvent the heavy computational load imposed by competing compressed sensing algorithms. Tom and Sheet [56] propose a method for generating B-mode images based on generative adversarial networks, which obviates the need for running expensive wave equation solvers. Luchies and Byram [57] apply Deep Learning to the problem of beamforming in ultrasound, for the purpose of minimizing off-axis scattering. Reiter and Bell [58] use a CNN to identify a common type of ultrasound artifact, namely the reflection artifact that arises when a small point-like target is embedded in the middle of an echogenic structure.

Finally, we note that Deep Learning has also been applied in non-reconstruction tasks to ultrasound, including classification [59], [60] and segmentation [61].

III. SIMULATIONS

Collecting real world ground truth data in quantities sufficient for training a neural network, is practically impossible. This leaves us with the alternative of using simulated data.

For training purposes, we have developed a simplified soft tissue model for organs and lesions. We model tissue as a uniform background with a mix of between one and five randomly selected ellipses, randomly selecting position, size and rotation using a uniform distribution. The sound speed for the background and each of the ellipses is randomly selected with uniform distribution in the range of 1300 m/s and 1800 m/s . Random speckle is added in the density domain, with a mean mass density of 0.9 g/cm^3 , uniformly distributed mass density variations between -3% and $+6\%$ and a mean distribution density of 2 reflectors per λ^2 . Attenuation is fixed at $0.5\text{ dB/(MHz}\cdot\text{cm)}$, or 2.5 dB/cm at the center frequency of 5 MHz . For the recovered domain we chose the central section, 1.875 cm wide by 3.75 cm deep. This is guided by two considerations: (1) coverage limitations due to maximum aperture size (2) the desire to show that our method can handle signals arriving from outside the recovered domain. The setup is depicted in Figure 2.

The numerical solver we work with is the k-wave toolbox for MATLAB [62], [63]. It presents a compromise that can deal with both discontinuities as well as speckle noise over non-uniform domains, while maintaining decent run times on an NVIDIA GPU.

We model the sensor based on our physical system, a Cephasonics ultrasound system, capable of transmitting on 64 channels at a time. The ultrasound probe is a 1D linear array transmitting at a central frequency of 5 MHz . The probe face is 3.75 cm wide and contains 128 elements. The probe plane is located just outside the PML with four grid points per Piezo

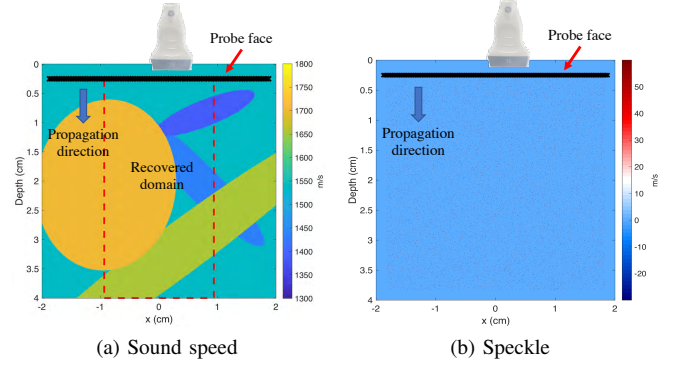


Fig. 2. Simulation setup. Reflecting objects are defined in the sound speed domain (a). Ultrasound speckle is defined in the density domain (b). The probe face is at the top end of the domain, marked by hash marks, and is outside the PML, propagation is towards the bottom. The recovered sound speed domain is marked by a red dashed line in (a).

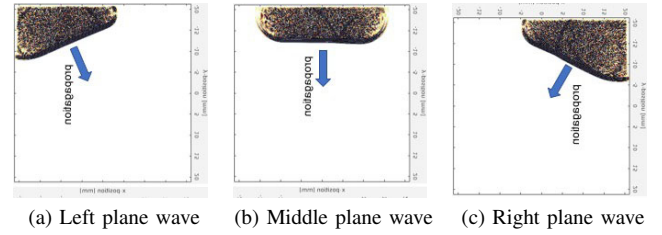


Fig. 3. The diagonal three plane waves generated in k-wave as well as by the real probe. Each plane wave is generated by 64 elements (half the probe), the limit of our current system.

element and an extra four grid points for the kerf. The total grid dimension is 4.24 cm by 4.24 cm .

For the transmit pattern we are limited by three parameters: simulation time, network resources, and signal to noise ratio (SNR). Both simulation time as well as network run time / resources are controlled by the number of pulses. In this work we use either one or three transmit pulses. This prevents us from using the classic scanning focused beam imaging approach. Due to SNR issues, using point source transmits, *i.e.* transmitting from a single element, is also problematic. As a result, we choose to work with three plane waves: one direct plane wave transmitted from the center of the probe, and two diagonal plane waves from the edges. These plane waves are depicted in Figure 2.

IV. NETWORK SETUP

We now describe the structure of our neural network. We wish to map signals to signals, hence we use a type of fully convolutional neural network (FCNN) - that is, there are no fully-connected layers, only convolutional layers, in addition to various non-linear activations. However, most FCNNs assume the input and output sizes are identical, whereas that is not the case in our setup. Therefore, we use striding within the convolutions in order to effectively achieve decimation.

Our base network architecture is depicted in Figure 4, and possesses an “hourglass” structure. In examining Figure 4, note the $C \times H \times W$ convention is used to describe the size of

the layer's output: that is, number of channel times height times width. The structure is referred to as hourglass due to its shape: in the initial layers (shown in orange in Figure 4), the resolution decreases, i.e. H and W both decrease; while the number of channels increases, from the initial 1, to 32, 64, 128, and finally 512. Thus, the layers get smaller but longer. In the second half of the network (shown in blue in Figure 4), the process is reversed: the resolution increases, while the number of channels goes down, finally reaching a single channel at the output. Thus, the layers get larger but shorter. Note that due to the input geometry and output aspect ratio, one linear interpolation step is required. This is due to the fact that the resolution increase is not a factor of two, going from a vertical resolution of 152 to 256.

We now describe the architecture in greater details, paying attention not just to the convolutional structure but also to the various activations used. On the downsampling path, the first four stages consist of a strided 3×3 convolution followed by batch normalization and a Relu operation. Note that the stride used is 2 in the width dimension, which has the effect of downsampling that dimension by a factor of 2. (In fact, the downsampling factor is sometimes not exactly 2; this is due to the nature of the convolutional padding used in the particular layer.) The following three stages consist of an ordinary (non-strided) 3×3 convolution followed by batch normalization, Relu and a 2×2 maxpool. The latter operation has the effect of reducing the resolution by a factor of 2 in both height and width dimensions (again, approximately, depending on the convolutional padding used). For the upsampling path, each of the first three stages consist of a 3×3 convolution followed by batch normalization, Relu and a $\times 2$ up-sampling. The fourth stage involves a 3×3 convolution followed by batch normalization, Relu and linear interpolation. The fifth stage is a 3×3 convolution followed by batch normalization, Relu (and no upsampling / interpolation). The final stage is a 1×1 convolution, which reduces the number of channels to one, and generates the output.

The base network shown in Figure 4 has the capability of dealing with a single plane-wave. We would like to use a variant of this base network for dealing with three plane-waves. Three different possibilities are depicted in Figure 5. In the ‘‘Start Network’’, the three plane waves are simply concatenated into a 3-channel image, and the remainder of the base network is identical. In the ‘‘Middle Network’’, the three plane-waves are each passed into identical subnetworks for the downsampling part of the base network; the results are then concatenated channel-wise, and then remainder of the upsampling part of the base network is the same. In the ‘‘End Network’’, the same idea is used, but the channel-wise concatenation only happens at the very end, prior to the 1×1 convolution. Note that for both Middle and End Networks, weight-sharing in the training phase ensures that each plane-wave is treated identically.

V. EXPERIMENTAL RESULTS

Let us now shift our attention to experimental validation. We will present results for both synthetic data as well as initial results for real data.

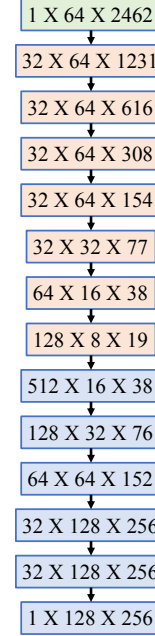


Fig. 4. Base network setup, for handling a single transmitted plane wave signal. The green layer denotes the input layer. Orange layers are the downsampling layers. Blue layers are the upsampling layers. Most steps involve a decrease or increase of resolution by a factor of two, except for the last upsampling step which is a linear interpolation stage to adapt the aspect ratio.

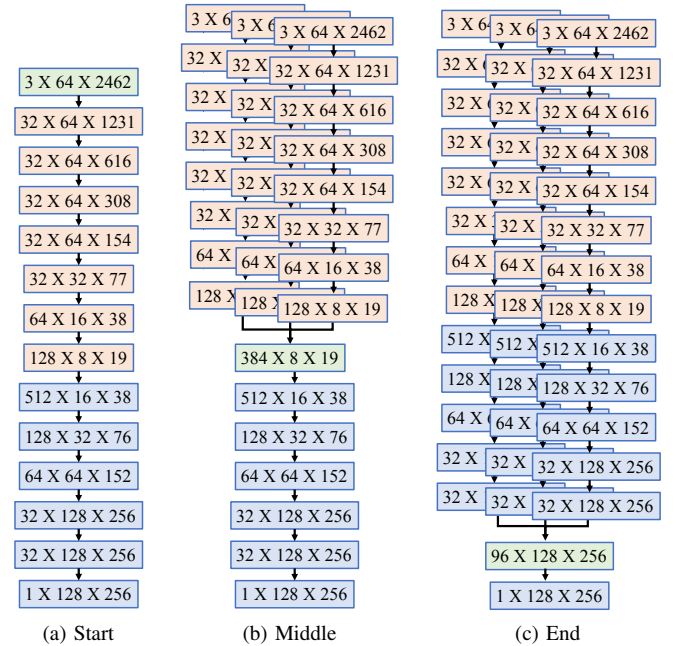


Fig. 5. Network configurations for dealing with the data from multiple plane waves (multiple transmissions). The green layer denotes the data concatenation layer. Orange layers are the downsampling layers. Blue layers are the upsampling layers.

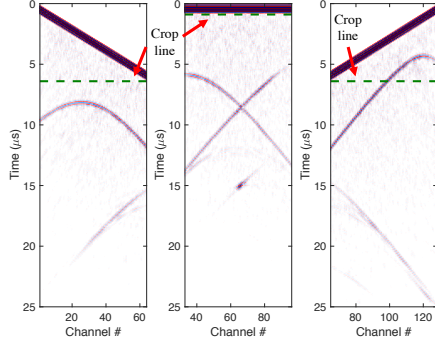


Fig. 6. Input channel data is cropped to remove the transmit pulse. The dashed green line shows the crop point for each of the plane waves. This is done to avoid signal saturation.

For the training of the neural network, we used the k-wave toolbox for Matlab to generate 6026 random training samples and 800 test samples using the procedure described in Sec III. Before feeding the data into the network, gain correction is applied at a rate of $0.48 \text{ dB}/\mu\text{s}$ ($2.5 \text{ dB}/\text{cm}$ at 1540 m/s). The channel data signals are then cropped in time to remove the transmit pulse, as depicted in Figure 6. This is done to remove the transmit signal that is several orders of magnitude stronger than the back-scattered signal, skewing signal statistics and results. Our physical system also suffers from electrical cross-talk in this temporal range during transmit, corrupting the data farther, as seen in Figure. 1a.

A. Results: synthetic data

Figure 7 presents reconstruction results on several samples from the test data. Recovery works well on larger objects but can miss fine details, as can be seen for example in image 16. Figure 8 shows absolute error values for the samples shown in Figure 7, with a threshold at 50 m/s . Another thing we can see is a slight misalignment at the edges. Consequently, although we do show the classic root mean square error (RMSE) values, it does not convey the full story. The RMSE norm is an L_2 norm, making it sensitive to outliers. Thus we also report mean and median absolute errors, which are less sensitive to outliers. Furthermore, to present error numbers which de-emphasize the issues due to localization around discontinuities, we further report the following modified error value: for each pixel, we take the minimum absolute error within a window with a radius of 5 pixels, for both the mean and median cases. For the mean error, in both cases both the mean absolute error (μ) as well as the standard deviation (σ) are reported. Results for all error measures are presented in Table III.

Available research suggests that for clinically relevant results, measurement accuracy on the order of 30 m/s is useful. All results are well within that range, and error measures that account for outliers at edges are an order of magnitude better. While more work is required to improve results on real data, we see very strong potential with our proposed technology.

We now turn to the issue of multiple inputs, that is, the use of multiple plane waves in image formation. While combining multiple inputs at the first layer (“Start Network”)

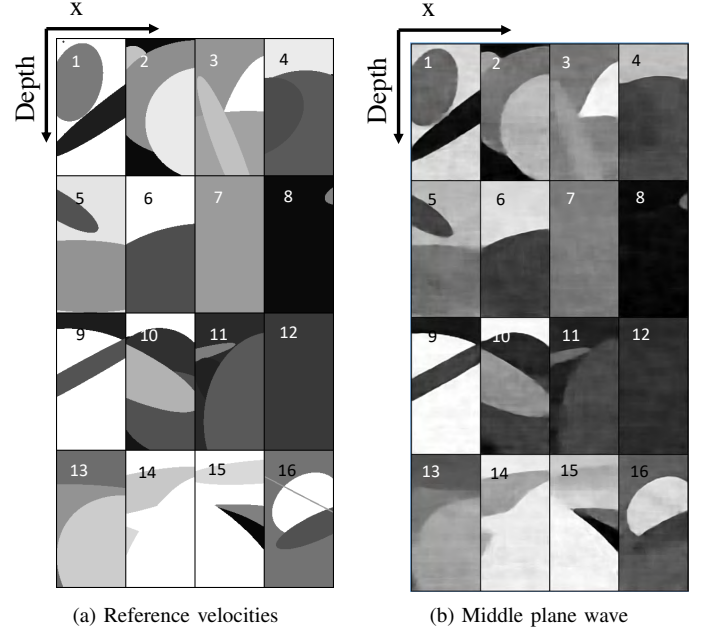


Fig. 7. Sound speed recovery maps on 16 test samples. Image (a) shows the ground truth data. Image (b) shows the sound speed maps recovered by the trained network using three plane waves and the “middle” network (see Figure 5). Gray scale values are in the range of 1300 m/s (black) to 1800 m/s (white).

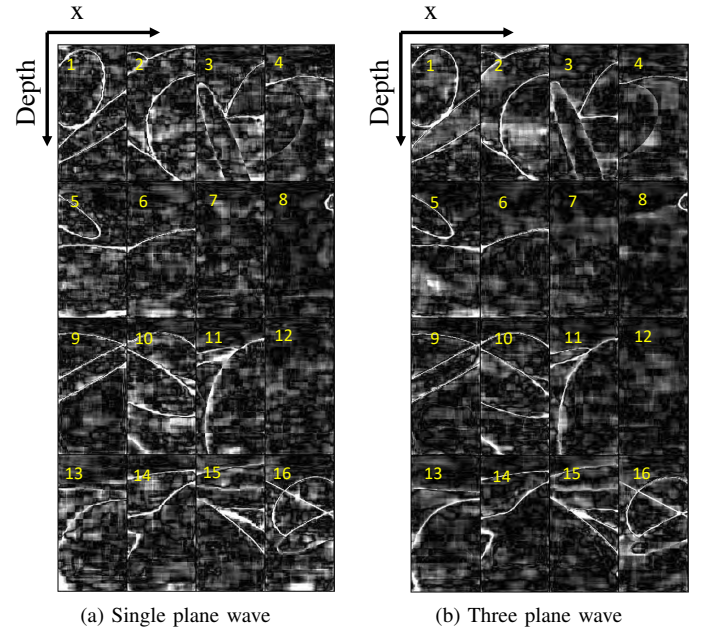


Fig. 8. Absolute error on 16 test samples. Error has been cropped at 50 m/s (white). Image (a) shows the results for the reconstruction using the single central plane wave. Image (b) shows the reconstruction using three plane waves and the “Middle” network (see Figure 5)

Network	Train							Test						
	RMSE	μ	σ	Median	μ^*	σ^*	Median*	RMSE	μ	σ	Median	μ^*	σ^*	Median*
Left	22.4	14.6	17.0	10.6	2.0	4.6	0.18	24.8	16.3	18.7	11.8	2.6	6.0	0.22
Center	23.3	15.1	17.8	10.7	2.5	5.7	0.19	25.2	16.2	19.3	11.4	3.1	7.0	0.24
Right	19.2	12.2	14.8	8.9	1.9	4.1	0.16	22.2	14.4	16.9	10.5	2.3	5.4	0.19
Start	21.8	14.2	16.9	10	2.4	5.4	0.19	24.3	15.6	18.6	11.0	2.9	6.5	0.23
Middle	18.8	11.5	14.9	8.2	2.1	4.3	0.17	20.5	12.5	16.1	8.7	2.6	5.2	0.21
End	18.9	11.9	14.8	8.5	1.6	3.7	0.14	20.8	12.9	16.3	9.0	2.0	5.0	0.16

TABLE III

RECONSTRUCTION ERROR FOR THE TRAIN AND TEST SETS FOR OUR SIX RECOVERY CASES: SINGLE PLANE WAVE RECONSTRUCTION FOR THE THREE PLANE WAVES, AND THREE PLANE WAVE RECONSTRUCTION FOR THE THREE JOINT RECONSTRUCTION NETWORKS (START, MIDDLE, END). ALL VALUES ARE IN METERS PER SECONDS. RMSE MEASURES THE ROOT MEAN SQUARE ERROR. μ AND σ DENOTE THE MEAN AND STANDARD DEVIATION VALUES FOR THE MEAN ABSOLUTE ERROR. MEDIAN SHOWS THE MEDIAN ABSOLUTE ERROR. THE STAR VALUES ARE FOR OUR MODIFIED ERROR VALUE, TAKING THE MINIMUM ABSOLUTE ERROR OVER A WINDOW WITH A RADIUS OF 5 PIXELS, FOR BOTH THE MEAN AND MEDIAN ERROR MEASURES.

does not improve reconstruction results, combining in both the middle (“Middle Network”) and the end (“End Network”) does provide some improvement, as can be seen Table III and Figure 8. However all cases are close to the recovery limit, so we expect more value in terms of stability to noise when dealing with real data.

B. Results: real data

For the case of real data, we look at three data-sets: (1) a polyurethane phantom with an inclusion (Fig. 9), (2) a cross section of the neck (Fig. 11) and (3) an image of the calf muscles (Gastrocnemius and Soleus, Fig 13). All these datasets were collected using a Cephasonics ultrasound system using a 128 linear probe transmitting at 5MHz. Both human scans were taken as part of a MIT Committee on the Use of Humans as Experimental Subjects (COUHES) approved protocol.

In addition to the sound speed images, we also collected shear wave velocity at the same location for comparison. Results for the polyurethane phantom are given in Fig. 10, the neck in Fig. 12 and the calf in Fig 14. Shear wave data was collected using a GE Logic E9 system with a GE 9L 192 element linear probe.

For the polyurethane phantom we have an approximate ground truth sound speed map, presented in Fig 9b, measured based on transmission travel time. Background sound speed is 1440 m/s and inclusion sound speed is 1750 m/s. Compared to the sound speed field reconstruction using a single plane wave (Fig 9c), we see that the near (top) side of the inclusion is detected correctly (with a slight velocity overshoot) but the bottom half is not. Sound speed close to the probe is under-estimated. Closer to the inclusion, sound speed is over-estimated, with large artifacts deeper into the phantom. In contrast, the three plane wave reconstruction shows significantly better results. The inclusion is fully detected, with an accuracy that is barely possible on the b-mode image. There are significantly fewer artifacts as well, but sound speed is still under estimated closer to the probe and over estimated close to the inclusion, although not as much as for the single plane-wave case.

The shear wave velocity map presented in Fig 10, shows that shear wave imaging does not fair well with this phantom. Although we do not have ground truth shear wave velocity maps, it is easy to see that the inclusion is not detected at

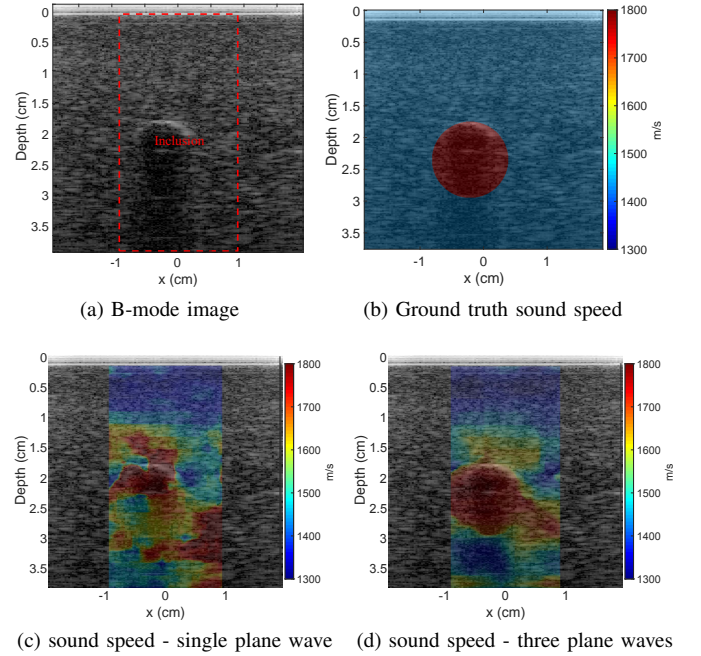


Fig. 9. Reconstruction on a polyurethane phantom with an inclusion. Image (a) shows a B-mode image reconstruction from point source data. Image (b) shows the ground truth sound speed mapped based on a background sound speed measurement of 1440 m/s, and inclusion sound speed measurement of 1750 m/s. Image (c) shows the sound speed reconstruction using the single central plane wave. Image (d) shows the sound speed reconstruction using three plane waves and the “Middle” network

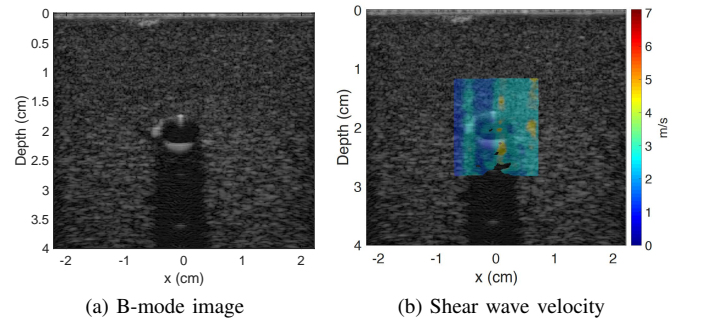


Fig. 10. Shear wave imaging of the polyurethane phantom presented in Fig. 9. Image (a) shows the b-mode image and image (b) shows the overlaid shear wave velocity map.

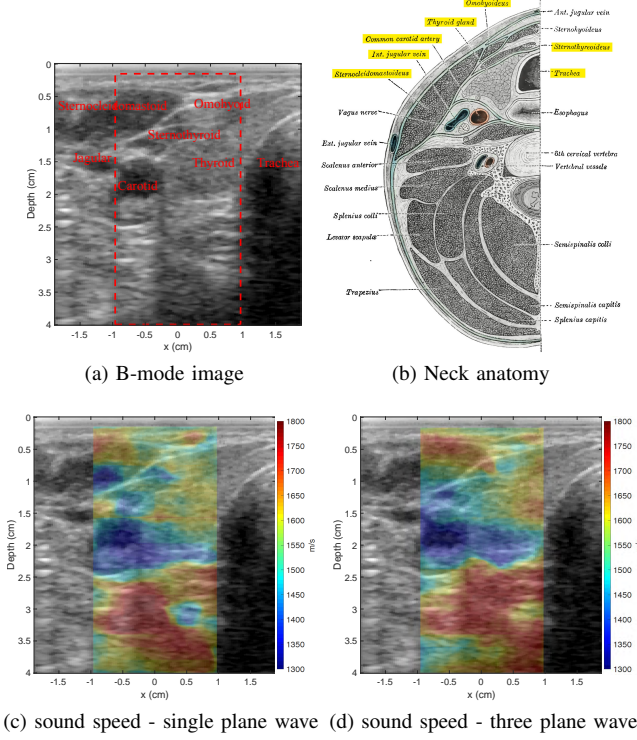


Fig. 11. Sound speed recovery for the neck. Image (a) shows a b-mode US image reconstruction. Image (b) shows an anatomical drawing of a cross section of the neck [64], with the anatomical landmarks appearing in (a) highlighted. Image (c) shows the sound speed reconstruction using the single central plane wave. Image (d) shows the sound speed reconstruction using three plane waves and the “Middle” network

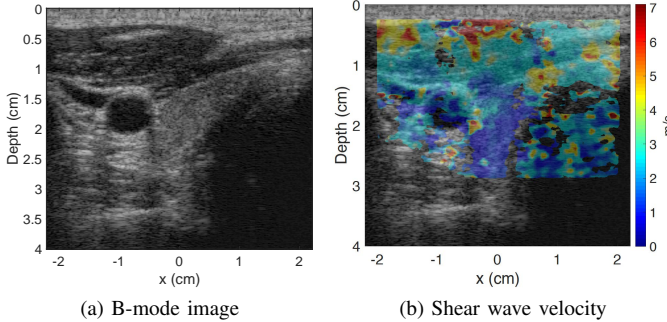


Fig. 12. Shear wave imaging of the neck, taken from the same angle of view presented in Fig. 11. Image (a) shows the b-mode image, image (b) shows the overlaid shear sound speed map.

all, and the sound speed map suffers from vertical artifacts, making the quality of these results questionable.

For the neck cross section sample, the annotated b-mode image is presented in Fig. 11a with the matching anatomical sketch in Fig. 11b. We do not have a ground truth sound speed map in this case to compare to, but we do see that the recovered sound speed map follows the anatomy, differentiating between muscle, carotid artery and thyroid gland. Additionally, the recovered sound speed map for the neck muscles (Sternocleidomastoid, Omohyoid and Sternothyroid) as well as the thyroid match the expected statistical values.

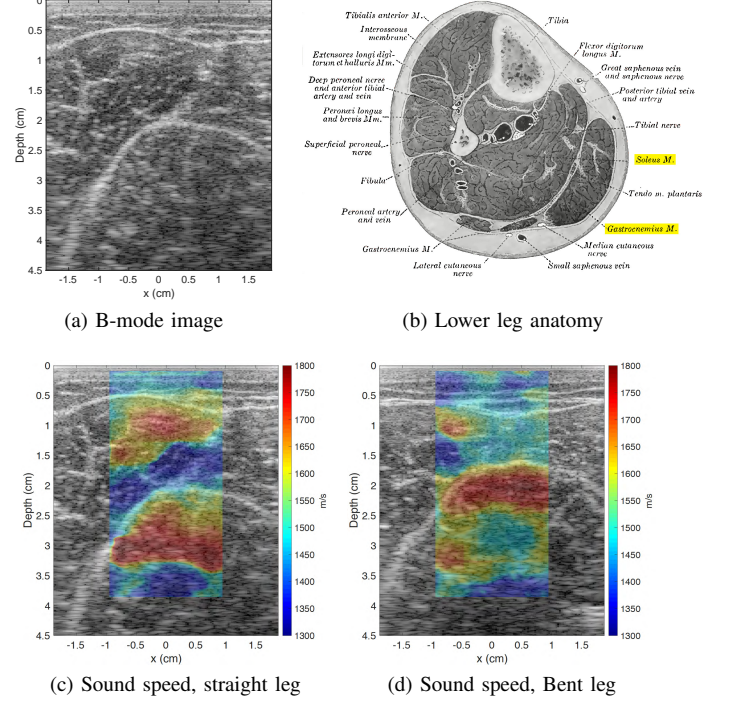


Fig. 13. Sound speed imaging of the lower leg muscle. Image (a) shows the b-mode US image reconstruction with the major muscles of interest delineated (Gastrocnemius and Soleus). Image (b) shows an anatomical sketch of a cross section of the lower leg [64]. Images (c) and (d) show sound speed reconstruction with toes in flexion, with a straight leg on the left, where we expect the GC to be active, and a bent leg on the right, where we expect the soleus to be active.

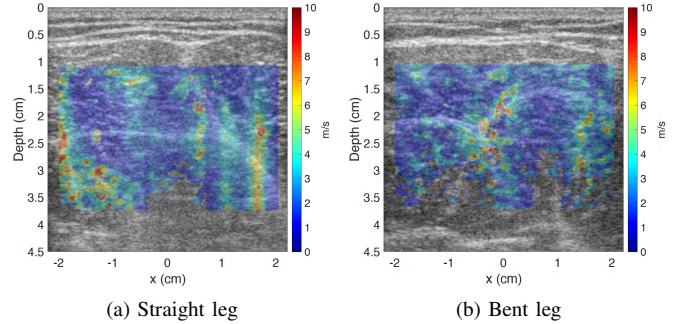


Fig. 14. Shear wave imaging of the leg matching Figs 13c and 13d respectively.

The deeper muscles are differentiated correctly anatomically but the sound speed does seem to be over estimated. In this, case, probably due to the higher feature density, there is a much smaller difference between the single plane-wave and three plane-wave versions. Turning our attention to the shear wave velocity image presented in Fig. 12, we can see that in this case, there is a general (though by no means perfect) correlation between the sound speed field generated by our network and the shear wave speed field. This correlation represents a general validation of our technique.

Finally, we turn our attention to a cross section scan of the calf muscles, specifically the Gastrocnemius and Soleus. Fig. 13a shows the annotated b-bode image and Fig. 13b

shows an anatomical sketch. In this case we explore functional imaging. Both sound speed maps are taken with the toes in flexion and under a small load to activate the calf muscles. The first frame, presented in Fig. 13c, shows an image with a straight leg, where we expect the Gastrocnemius (external muscle) to be the main active muscle. The second frame, shown in Fig. 13d, shows the results with a bent leg, where we expect the Soleus (internal muscle) to be the one doing most of the work. The contraction of the Gastrocnemius muscle is very obvious, although in the case where it is contracting, it appears that the lower half is estimated as having a low sound speed instead of high. The response of the Soleus is not as obvious, as sound speed estimation is too high in both cases, but can still be observed in the results.

As before, shear wave velocity images are presented for both cases in Fig 14. As is easily seen, these results do not provide any meaningful information. In fact, it is our general experience that full frame shear wave velocity images on loaded muscles tend to be highly unstable at best, especially when looking at cross section slices. Based on our experience as well as results reported by other researchers, better results can be achieved when using a very limited field of view to increase frame rates combined with transverse probe positioning so that the shear waves propagate along the muscle fibers. However, in that case we lose the bigger picture regarding which parts of the muscle are activating, and the potential frame rate is still much more limited.

VI. CONCLUSIONS AND FUTURE WORK

In this paper we presented a Deep Learning framework for the recovery of sound speed maps from plane wave ultrasound channel data. Results on synthetic data are more than an order of magnitude better than our target accuracy, showing that this framework has great potential for clinical purposes.

Initial real data results are also highly encouraging, although more research is required in order to improve the results, create calibrated phantoms for validation and improve training as well as develop better simulation techniques to better train the network to deal with real data.

REFERENCES

- [1] H. Y.-H. Lin, Y.-L. Lee, K.-D. Lin, Y.-W. Chiu, S.-J. Shin, S.-J. Hwang, H.-C. Chen, and C.-C. Hung, "Association of Renal Elasticity and Renal Function Progression in Patients with Chronic Kidney Disease Evaluated by Real-Time Ultrasound Elastography," *Scientific Reports*, vol. 7, Feb. 2017.
- [2] H. Singh, O. B. Panta, U. Khanal, and R. K. Ghimire, "Renal Cortical Elastography: Normal Values and Variations," *Journal of Medical Ultrasound*, vol. 25, no. 4, pp. 215–220, Dec. 2017.
- [3] J. Carlsen, C. Ewertsen, L. Lönn, and M. Nielsen, "Strain Elastography Ultrasound: An Overview with Emphasis on Breast Cancer Diagnosis," *Diagnostics*, vol. 3, no. 1, pp. 117–125, 2013.
- [4] J. M. Chang, J.-K. Won, K.-B. Lee, I. A. Park, A. Yi, and W. K. Moon, "Comparison of shear-wave and strain ultrasound elastography in the differentiation of benign and malignant breast lesions," *American Journal of Roentgenology*, vol. 201, no. 2, pp. W347–W356, Aug. 2013, 00074.
- [5] R. G. Barr, G. Ferraioli, M. L. Palmeri, Z. D. Goodman, G. Garcia-Tsao, J. Rubin, B. Garra, R. P. Myers, S. R. Wilson, D. Rubens, and D. Levine, "Elastography Assessment of Liver Fibrosis: Society of Radiologists in Ultrasound Consensus Conference Statement," *Radiology*, vol. 276, no. 3, pp. 845–861, Sep. 2015.
- [6] G. Ferraioli, P. Parekh, A. B. Levitov, and C. Filice, "Shear Wave Elastography for Evaluation of Liver Fibrosis," *Journal of Ultrasound in Medicine*, vol. 33, no. 2, pp. 197–203, Feb. 2014.
- [7] J. F. Greenleaf, M. Fatemi, and M. Insana, "Selected methods for imaging elastic properties of biological tissues," *Annual Review of Biomedical Engineering*, vol. 5, no. 1, pp. 57–78, Aug. 2003.
- [8] Kathy Nightingale, "Acoustic Radiation Force Impulse (ARFI) Imaging: A Review," *Current Medical Imaging Reviews*, vol. 7, no. 4, pp. 328–339, Nov. 2011.
- [9] J. L. Gennisson, T. Defieux, and M. Fink, "Ultrasound elastography: Principles and techniques," *Diagnostic and Interventional Imaging*, vol. 94, no. 5, pp. 487–495, 2013.
- [10] J. Bercoff, M. Tanter, and M. Fink, "Supersonic Shear Imaging : A New Technique for Soft Tissue Elasticity Mapping," *IEEE Transactions on Ultrasonics, Ferroelectrics and Frequency Control*, vol. 51, no. 4, pp. 396–409, 2004.
- [11] A. Nahas, M. Tanter, T.-M. Nguyen, J.-M. Chassot, M. Fink, and a. Claude Boccara, "From supersonic shear wave imaging to full-field optical coherence shear wave elastography," *Journal of biomedical optics*, vol. 18, no. 12, p. 121514, 2013.
- [12] M. S. Farvid, T. W. K. Ng, D. C. Chan, P. H. R. Barrett, and G. F. Watts, "Association of adiponectin and resistin with adipose tissue compartments, insulin resistance and dyslipidaemia," *Diabetes, Obesity and Metabolism*, vol. 7, no. 4, pp. 406–413, Jul. 2005.
- [13] J. Oudry, C. Bastard, V. Miette, R. Willinger, and L. Sandrin, "Copolymer-in-oil Phantom Materials for Elastography," *Ultrasound in Medicine and Biology*, vol. 35, no. 7, pp. 1185–1197, 2009.
- [14] O. Roy, I. Jovanović, A. Hormati, R. Parhizkar, and M. Vetterli, "Sound speed estimation using wave-based ultrasound tomography: Theory and GPU implementation," in *SPIE Medical Imaging*, J. D'hooge and S. A. McAleavey, Eds., San Diego, California, USA, Mar. 2010, p. 76290J.
- [15] C. Li, A. Stewart, and N. Duric, "Multi-grid tomographic inversion for breast ultrasound imaging," *Proceedings of SPIE*, vol. 8320, pp. 1–9, 2012.
- [16] T. Hopp, N. V. Ruiter, and N. Duric, "Breast tissue characterization by sound speed: Correlation with mammograms using a 2D/3D image registration," in *2012 IEEE International Ultrasonics Symposium*, Oct. 2012, pp. 1–4.
- [17] J. Nebeker and T. R. Nelson, "Imaging of Sound Speed Using Reflection Ultrasound Tomography," *Journal of Ultrasound in Medicine*, vol. 31, no. 9, pp. 1389–1404, Sep. 2012.
- [18] N. Duric, P. Littrup, S. Schmidt, C. Li, O. Roy, L. Bey-Knight, R. Janer, D. Kunz, X. Chen, J. Goll, A. Wallen, F. Zafar, V. Allada, E. West, I. Jovanovic, and K. Greenway, "Breast imaging with the SoftVue imaging system: First results," *Medical Imaging 2013: Ultrasonic Imaging, Tomography, and Therapy*, vol. 8675, p. 86750K, 2013.
- [19] C. Li, G. S. Sandhu, O. Roy, N. Duric, V. Allada, and S. Schmidt, "Toward a practical ultrasound waveform tomography algorithm for improving breast imaging," in *Medical Imaging 2014: Ultrasonic Imaging and Tomography*, vol. 9040, 2014, p. 90401P.
- [20] M. Sak, N. Duric, P. Littrup, L. Bey-Knight, H. Ali, P. Vallieres, M. E. Sherman, and G. L. Gierach, "Using speed of sound imaging to characterize breast density," *Ultrasound in medicine & biology*, vol. 43, no. 1, pp. 91–103, Jan. 2017.
- [21] J. R. Fincke, M. Feigin, G. A. Prieto, X. Zhang, and B. Anthony, "Towards ultrasound travel time tomography for quantifying human limb geometry and material properties," in *SPIE Medical Imaging*, N. Duric and B. Heyde, Eds., Apr. 2016, p. 97901S.
- [22] J. R. Fincke, "Imaging cortical bone using the level-set method to regularize travel-time and full waveform tomography techniques," *The Journal of the Acoustical Society of America*, vol. 141, no. 5, pp. 3549–3549, May 2017.
- [23] M. E. Anderson and G. E. Trahey, "The direct estimation of sound speed using pulse-echo ultrasound," *The Journal of the Acoustical Society of America*, vol. 104, no. 5, pp. 3099–3106, Nov. 1998.
- [24] H. Hachiya, S. Ohtsuki, M. Tanaka, and F. Dunn, "Determination of sound speed in biological tissues based on frequency analysis of pulse response," *The Journal of the Acoustical Society of America*, vol. 92, no. 3, pp. 1564–1568, Sep. 1992.
- [25] H.-C. Shin, R. Prager, H. Gomersall, N. Kingsbury, G. Treece, and A. Gee, "Estimation of Speed of Sound using Medical Ultrasound Image Deconvolution," *Ultrasonics*, vol. 50, no. 7, p. 24, Jun. 2010.
- [26] Alex Benjamin, Rebecca E. Zubajlo, Manish Dhyani, Anthony E. Samir, Kai E. Thomenius, Joseph R. Grajo, and Brian W. Anthony, "Surgery for Obesity and Related Diseases: I. A Novel Approach to the Quantification of the Longitudinal Speed of Sound and Its Potential for

- Tissue Characterization,” *Ultrasound in Medicine and Biology*, vol. 44, no. 12, pp. 2739–2748, Dec. 2018.
- [27] R. E. Zubajlo, A. Benjamin, J. R. Grajo, K. Kaliannan, J. X. Kang, Atul K. Bhan, Kai E. Thomenius, Brian W. Anthony, Manish Dhyani, and Anthony E. Samir, “Surgery for obesity and related diseases: II. Experimental validation of longitudinal speed of sound estimates in the diagnosis of hepatic steatosis,” *Ultrasound in Medicine & Biology*, vol. 44, no. 12, pp. 2749–2758, Dec. 2018.
- [28] A. Samani, J. Zubovits, and D. Plewes, “Elastic moduli of normal and pathological human breast tissues: An inversion-technique-based investigation of 169 samples,” *Physics in medicine and biology*, vol. 52, no. 6, pp. 1565–1576, 2007.
- [29] Y.-C. Fung, *Biomechanics: Mechanical Properties of Living Tissues*. New York, NY: Springer New York, 1993.
- [30] H. Hachiya, S. Ohtsuki, and M. Tanaka, “Relationship Between Speed of Sound in and Density of Normal and Diseased Rat Livers,” *Japanese Journal of Applied Physics*, vol. 33, no. 5S, p. 3130, 1994.
- [31] T. Matsuhashi, N. Yamada, H. Shinzawa, and T. Takahashi, “An evaluation of hepatic ultrasound speed in injury models in rats: Correlation with tissue constituents,” *Journal of Ultrasound in Medicine*, vol. 15, no. 8, pp. 563–570, Aug. 1996.
- [32] C. Li, N. Duric, P. Littrup, and L. Huang, “In vivo breast sound-speed imaging with ultrasound tomography,” *Ultrasound Med Biol*, vol. 35, no. 10, pp. 1615–1628, 2009.
- [33] M. Imbault, A. Faccinnetto, B.-F. Osmanski, A. Tissier, T. Deffieux, J.-L. Gennisson, V. Vilgrain, and M. Tanter, “Robust sound speed estimation for ultrasound-based hepatic steatosis assessment,” *Physics in Medicine and Biology*, vol. 62, no. 9, pp. 3582–3598, May 2017.
- [34] A. Benjamin, R. Zubajlo, K. Thomenius, M. Dhyani, K. Kaliannan, A. E. Samir, and B. W. Anthony, “Non-invasive diagnosis of non-alcoholic fatty liver disease (NAFLD) using ultrasound image echogenicity,” in *2017 39th Annual International Conference of the IEEE Engineering in Medicine and Biology Society (EMBC)*. Seogwipo: IEEE, Jul. 2017, pp. 2920–2923.
- [35] X. Wang, Y. Peng, L. Lu, Z. Lu, M. Bagheri, and R. M. Summers, “Chestx-ray8: Hospital-scale chest x-ray database and benchmarks on weakly-supervised classification and localization of common thorax diseases,” in *Computer Vision and Pattern Recognition (CVPR), 2017 IEEE Conference on*. IEEE, 2017, pp. 3462–3471.
- [36] M. F. Byrne, F. Soudan, M. Henkel, C. Oertel, N. Chapados, F. J. Echagüe, S. H. Ghalehjeh, N. Guizard, S. Giguère, M. E. MacPhail *et al.*, “Mo1679 real-time artificial intelligence full colonoscopy workflow for automatic detection followed by optical biopsy of colorectal polyps,” *Gastrointestinal Endoscopy*, vol. 87, no. 6, p. AB475, 2018.
- [37] M. Havaei, A. Davy, D. Warde-Farley, A. Biard, A. Courville, Y. Bengio, C. Pal, P.-M. Jodoin, and H. Larochelle, “Brain tumor segmentation with deep neural networks,” *Medical image analysis*, vol. 35, pp. 18–31, 2017.
- [38] Y. Zhang and H. Yu, “Convolutional neural network based metal artifact reduction in x-ray computed tomography,” *IEEE transactions on medical imaging*, vol. 37, no. 6, pp. 1370–1381, 2018.
- [39] Q. Yang, P. Yan, Y. Zhang, H. Yu, Y. Shi, X. Mou, M. K. Kalra, Y. Zhang, L. Sun, and G. Wang, “Low dose ct image denoising using a generative adversarial network with wasserstein distance and perceptual loss,” *IEEE transactions on medical imaging*, 2018.
- [40] E. Kang, W. Chang, J. Yoo, and J. C. Ye, “Deep convolutional framelet denoising for low-dose ct via wavelet residual network,” *IEEE transactions on medical imaging*, vol. 37, no. 6, pp. 1358–1369, 2018.
- [41] Z. Zhang, X. Liang, X. Dong, Y. Xie, and G. Cao, “A sparse-view ct reconstruction method based on combination of densenet and deconvolution,” *IEEE transactions on medical imaging*, vol. 37, no. 6, pp. 1407–1417, 2018.
- [42] Y. Han and J. C. Ye, “Framing u-net via deep convolutional framelets: Application to sparse-view ct,” *IEEE transactions on medical imaging*, vol. 37, no. 6, pp. 1418–1429, 2018.
- [43] X. Zheng, S. Ravishankar, Y. Long, and J. A. Fessler, “Pwls-ultra: An efficient clustering and learning-based approach for low-dose 3d ct image reconstruction,” *IEEE transactions on medical imaging*, vol. 37, no. 6, pp. 1498–1510, 2018.
- [44] H. Shan, Y. Zhang, Q. Yang, U. Kruger, W. Cong, and G. Wang, “3d convolutional encoder-decoder network for low-dose ct via transfer learning from a 2d trained network,” *IEEE transactions on medical imaging*, vol. 37, no. 6, pp. 1522–1534, 2018.
- [45] G. Yang, S. Yu, H. Dong, G. Slabaugh, P. L. Dragotti, X. Ye, F. Liu, S. Arridge, J. Keegan, Y. Guo *et al.*, “Dagan: Deep de-aliasing generative adversarial networks for fast compressed sensing mri reconstruction,” *IEEE transactions on medical imaging*, vol. 37, no. 6, pp. 1310–1321, 2018.
- [46] B. Gözcü, R. K. Mahabadi, Y.-H. Li, E. Ilıcak, T. Cukur, J. Scarlett, and V. Cevher, “Learning-based compressive mri,” *IEEE transactions on medical imaging*, vol. 37, no. 6, pp. 1394–1406, 2018.
- [47] T. M. Quan, T. Nguyen-Duc, and W.-K. Jeong, “Compressed sensing mri reconstruction using a generative adversarial network with a cyclic loss,” *IEEE transactions on medical imaging*, vol. 37, no. 6, pp. 1488–1497, 2018.
- [48] B. Yang, L. Ying, and J. Tang, “Artificial neural network enhanced bayesian pet image reconstruction,” *IEEE transactions on medical imaging*, 2018.
- [49] K. Kim, D. Wu, K. Gong, J. Dutta, J. H. Kim, Y. D. Son, H. K. Kim, G. El Fakhri, and Q. Li, “Penalized pet reconstruction using deep learning prior and local linear fitting,” *IEEE transactions on medical imaging*, vol. 37, no. 6, pp. 1478–1487, 2018.
- [50] A. Hauptmann, F. Lucka, M. Betcke, N. Huynh, J. Adler, B. Cox, P. Beard, S. Ourselin, and S. Arridge, “Model-based learning for accelerated, limited-view 3-d photoacoustic tomography,” *IEEE transactions on medical imaging*, vol. 37, no. 6, pp. 1382–1393, 2018.
- [51] D. Allman, A. Reiter, and M. A. L. Bell, “Photoacoustic source detection and reflection artifact removal enabled by deep learning,” *IEEE transactions on medical imaging*, vol. 37, no. 6, pp. 1464–1477, 2018.
- [52] A. Mousavi, G. Dasarathy, and R. G. Baraniuk, “Deepcode: Adaptive sensing and recovery via deep convolutional neural networks,” *arXiv preprint arXiv:1707.03386*, 2017.
- [53] C. A. Metzler, P. Schniter, A. Veeraraghavan, and R. G. Baraniuk, “prdeep: Robust phase retrieval with flexible deep neural networks,” *arXiv preprint arXiv:1803.00212*, 2018.
- [54] S. Vedula, O. Senouf, A. M. Bronstein, O. V. Mikhailovich, and M. Zibulevsky, “Towards CT-quality Ultrasound Imaging using Deep Learning,” *arXiv:1710.06304 [physics]*, Oct. 2017, 00000.
- [55] Y. H. Yoon, S. Khan, J. Huh, and J. C. Ye, “Efficient B-mode Ultrasound Image Reconstruction from Sub-sampled RF Data using Deep Learning,” *arXiv:1712.06096 [cs, stat]*, Dec. 2017.
- [56] F. Tom and D. Sheet, “Simulating patho-realistic ultrasound images using deep generative networks with adversarial learning,” in *Biomedical Imaging (ISBI 2018), 2018 IEEE 15th International Symposium on*. IEEE, 2018, pp. 1174–1177.
- [57] A. C. Luchies and B. C. Byram, “Deep Neural Networks for Ultrasound Beamforming,” *IEEE Transactions on Medical Imaging*, pp. 1–1, 2018, 00005.
- [58] A. Reiter and M. A. Lediju Bell, “A machine learning approach to identifying point source locations in photoacoustic data,” in *Photons Plus Ultrasound: Imaging and Sensing*, A. A. Oraevsky and L. V. Wang, Eds., Mar. 2017, p. 100643J, 00000.
- [59] H. Ravishankar, P. Sudhakar, R. Venkataramani, S. Thiruvankadam, P. Annangi, N. Babu, and V. Vaidya, “Understanding the mechanisms of deep transfer learning for medical images,” in *Deep Learning and Data Labeling for Medical Applications*. Springer, 2016, pp. 188–196.
- [60] Q. Zheng, G. Tastan, and Y. Fan, “Transfer learning for diagnosis of congenital abnormalities of the kidney and urinary tract in children based on ultrasound imaging data,” in *Biomedical Imaging (ISBI 2018), 2018 IEEE 15th International Symposium on*. IEEE, 2018, pp. 1487–1490.
- [61] M. Xian, Y. Zhang, H.-D. Cheng, F. Xu, K. Huang, B. Zhang, J. Ding, C. Ning, and Y. Wang, *A Benchmark for Breast Ultrasound Image Segmentation (BUSIS)*. Infinite Study, 2018.
- [62] B. E. Treeby and B. T. Cox, “K-Wave: MATLAB toolbox for the simulation and reconstruction of photoacoustic wave fields,” *Journal of Biomedical Optics*, vol. 15, no. 2, p. 021314, 2010.
- [63] B. E. Treeby, J. Jaros, D. Rohrbach, and B. T. Cox, “Modelling elastic wave propagation using the k-wave matlab toolbox,” in *Ultrasonics Symposium (Ius), 2014 Ieee International*. IEEE, 2014, pp. 146–149, 00016.
- [64] H. Gray and W. H. Lewis, *Anatomy of the Human Body*, 20th ed. Lea & Febiger, 1918.